Draft version August 31, 2025
Typeset using LaTeX **twocolumn** style in AASTeX7

The shock-induced chemistry of dust formation in the colliding winds of Wolf-Rayet stars

Erica Messmer,[1] Arkaprabha Sarangi,[2] and Shazrene Mohamed[3]

[1] *University of Illinois, Astronomy Building, 1002 W Green St Urbana IL 61801*
[2] *Indian Institute of Astrophysics, 100 Feet Rd, Koramangala, Bengaluru, Karnataka 560034, India*
[3] *University of Virginia, Astronomy Building, 530 McCormick Road, Charlottesville, VA 22904, USA*

ABSTRACT

A number of Wolf-Rayet (WR) stars in binary systems show significant dust production, either as continuous spirals of dust or dramatic concentric arcs. This dust production is believed to be a product of the colliding winds of the binary, and much work is being done to understand the exact mechanisms of dust formation in these systems. Unbroken spirals point to continuous dust production and are understood to be related to systems with very circular orbits, as in the 'pinwheel nebula' WR104. Concentric arcs are believed to be found in systems with high eccentricity orbits, as in WR140. We study the dust formation in the case of both continuous and episodic dust producing WR binaries, taking WR104 and WR140 as the canonical examples of these systems. We focus on the chemical pathways available for dust formation, developing a 1D model describing the dynamics of the gas in the wind collision region and coupling these results with a chemical-kinetic dust formation code. Our 1D results are informed by snapshots of a 3D `Arepo` hydrodynamic simulation of the binary. Preliminary results are presented, where we find that gas of pure WR star abundances rapidly forms a large amount of amorphous carbon dust, with a small amount of silicates able to form at much later times. A gas of pure OB star abundances forms no such carbon dust, and instead forms multiple species of silicates. The formation of dust in the pure OB case is found to occur at distances much too large to agree with observations, indicating that some amount of mixing is necessary to reproduce the observed dust formation. Continuing work on this project includes running our dust production models for the case of fully mixed WR and OB gas, and determining the dust mass produced in all cases.

1. INTRODUCTION

Wolf-Rayet (WR) stars are an observational category, describing stars whose spectra show very broad emission lines and a distinct lack of H features (White and Tuthill 2024). Many WR are massive stars entering the end phases of their lives and stripping their H envelope, either via strong line-driven winds or due to mass transfer onto a companion (Shenar et al. 2020). These massive stars are extremely luminous and hot, with effective temperatures in the range of 20-30 K, driving powerful winds with speeds $\sim$ 1000s km/s. These winds cause continuous mass loss, with rates on the order of $10^{-8} - 10^{-6} M_{\odot}$/yr (Crowther 2007). WR are typically found as part of binary systems, with at least 50% of WR having an OB companion (Shenar et al. 2020). The strong radiation and winds of two massive stars would seem to provide ideal conditions to completely inhibit dust formation, however, we see considerable dust production occurring in many WR binary systems, detected by a constant or episodic excess infrared flux (Gehrz and Hackwell 1974; Williams et al. 1987). Dust formation is typically seen in the cooler and carbon-rich WR classes (WC), where they are estimated to produce large amounts of carbon rich dust, $\dot{M}_d$ $10^{-10} - 10^{-6} M_{\odot} yr^{-1}$ (Zubko 1998).

This dust production can be explained by shocks generated by the wind collision region between the two stars, and these systems are known as Colliding Wind Binaries (CWB). The geometries and orbital parameters of the systems determine when and where dust is able to form. CWBs with more circular orbits are seen to produce dust continuously, with the canonical example being WR104, or the Pinwheel Nebula (Kato et al. 2002; Soulain et al. 2018). Those systems with a more eccentric orbit produce dust only periodically, when the stars are near periastron. The prototypical example of these periodic dust producers is WR140 (Williams et al. 1990; Lau et al. 2023). Dust formation thus appears to depend on the separation distance between the stars, and obser-

Email: albrigo2@illinois.edu

vations indicate that dust forms relatively close to the companions, typically ~ 10s of AU (Lau et al. 2020). Dust formation occurring in these regions, which would still be subject to the strong radiation from both stars, requires that there be both strong density compression in the colliding wind shocks, and strong radiative cooling. The initial formation mechanisms for this dust are not well understood, and the known dust-producing WR binaries are located at distances from ~ 1-10 kpc (Rosslowe and Crowther 2015) meaning that resolution of the innermost wind collision region is impossible, necessitating simulation and modeling to understand the nascent dust formation.

A description of the dynamical processes allowing for dust production is an important aspect of understanding the early formation, but it must be considered along with the chemical pathways allowing for the nucleation of dust grain precursors from the gas phase. Observations indicate that the primary component of WC dust is best fit by amorphous carbon (AC) grains (Williams et al. 1987; Williams 1997), and indeed early modeling of dust nucleation indicated that AC grains form readily in these systems while silicate grains struggle to form, likely due to the H deficient environment of a stripped envelope star (Cherchneff et al. 2000). This work will build on studies of the dynamical processes required for dust formation in WR binaries, such as Eatson et al. (2022); Harries et al. (2004) as well as work on the chemical formation scenarios in Cherchneff et al. (2000). We will use two systems as 'canonical' examples of episodic vs continuous dust producers: WR140 and WR104.For this initial study, we consider a 1D model which is described in section 2. We describe the dust precursor formation pathways followed by our results in section 3 and discussion in 4.

2. METHODOLOGY

2.1. *Wind Collision Region*

Figure 1 shows a schematic of the structures in a WR binary system. The two strong stellar winds of the WR and its OB companion are accelerated to their terminal velocities of order a few × 1e3 km/s. These winds will interact and form two opposite-facing shocks separated by a contact discontinuity. The location of this interaction depends on the orbital parameters of the system and the wind momentum ratio, η. This ratio is defined as:

$$\eta = \frac{\dot{M}_{\mathrm{OB}} v_{\mathrm{OB}}^{\infty}}{\dot{M}_{\mathrm{WR}} v_{\mathrm{WR}}^{\infty}} \tag{1}$$

While the winds from the OB companion are typically faster, the greater mass loss of the WR means that in our systems of interest η is very small, thus the WR winds dominate. Using this momentum ratio and assuming that both stellar winds are spherical and isotropic, we can then use the ram pressure balance condition to determine where the winds will meet and form the contact discontinuity (CD). The interaction location is described in term of r_{OB} and r_{WR}, the distances from the OB and WR stars respectively, to this wind collision region:

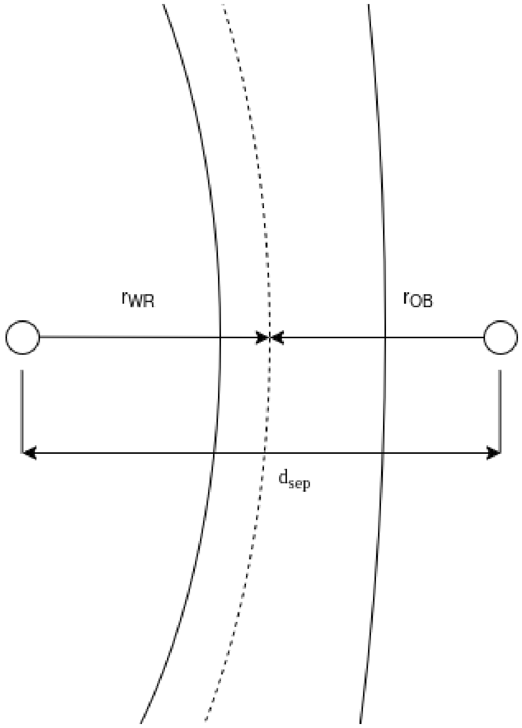

Figure 1. Schematic of the colliding winds. The contact discontinuity (dashed line) is curved towards the star with the weaker wind, as are the shocks (solid lines). The stars are separated by a distance d_{sep}, and the distance from each star to the contact are r_{WR} and r_{OB}.

$$r_{OB} = \frac{\eta^{1/2}}{1+\eta^{1/2}} d_{sep} \qquad r_{WR} = \frac{1}{1+\eta^{1/2}} d_{sep}$$

Where d_{sep} is the separation distance between the stars. This formalism assumes that the winds emerge from stationary points, which is of course not strictly the case as the stars are in orbit around each other. However, we can neglect the orbital motion because the orbital velocity is many times smaller than the wind velocity. Following Stevens et al. (1992), and taking WR 140 as an example, we can estimate the orbital velocity v_{orb} in [km/s] as $v_{orb} \sim 210[(M_1 + M_2)/P_{orb}]^{1/3}$, taking the stellar masses in $M_{\odot}$ and P_{orb} in days. For WR 140, the orbital velocity is ~ 50 km/s, multiple orders of magnitude smaller than the wind velocities.

System		Parameter	Source
WR 140			
	P	2895 days	Thomas et al. (2021)
	e	0.899	Thomas et al. (2021)
	a	13.55 AU	Thomas et al. (2021)
	$r_{\rm peri}$	1.3	Williams (2011)
WR 104			
	P	241.5 days	Tuthill et al. (2008)
	e	0.06	Tuthill et al. (2008)
	a	2.34 AU	Lamberts et al. (2012)
	$r_{\rm peri}$	2.19 AU	

Table 1. Orbital parameters adopted here for WR140 and WR104.

To determine the the location of the contact discontinuity for our specific systems of interest, we adopt the values given in Table 1.

It is within this interaction region that the gas can be compressed and cooled by the shocks to reach conditions allowing for dust formation. This is true if the shocks are radiative rather than adiabatic. To determine in which situations this is the case, we can examine how the cooling time of the gas, $t_{\rm cool}$ compares to how long it takes the gas to move out of the shocked flow, the escape time $t_{\rm esc}$. For an order of magnitude estimation, one can approximate the cooling time as:

$$t_{\rm cool} \propto \frac{kT_s}{n\Lambda(T_s)} \tag{2}$$

Where T_s is the temperature of the shocked wind, n is the number density of the gas, and $\Lambda(T_s)$ is the value of the cooling function at this temperature. We can approximate $\Lambda(T_s)$ as a locally constant value, as the shock temperatures in CWBs occur near a plateau in the cooling function, visible in Figure 2. One then defines an escape time, using the distance from the star to the contact discontinuity, d_c and the speed of sound in the post-shock gas, c_s:

$$t_{esc} \propto \frac{d_c}{c_s} \tag{3}$$

We then define a parameter χ:

$$\chi = \frac{t_{\rm cool}}{t_{esc}} \approx \frac{v_8^4 d_{12}}{\dot{M}_{-7}} \tag{4}$$

Where v_8 is the wind velocity in units of 1000 km s^{-1}, d_{12} is the distance to the contact discontinuity in units of 10^7 km, and $\dot{M}_{-7}$ is the mass loss rate in units of $10^{-7} M_\odot$ yr^{-1}

Parkin and Pittard (2008) shows that in hydrodynamic simulations, shocks behave adiabatically if $\chi \gtrsim 3$ and radiatively if $\chi \lesssim 3$. For our cases, we find that WR 104 has $\chi \sim 0.9$ and WR 140 at perihelion has $\chi \sim 2$, compared to WR 140 at aphelion with $\chi \sim 30$. Thus, we expect the shocks to behave radiatively for WR104 throughout its orbit, and for WR140 near and during periastron. A description of the shock jump conditions, and our methodology for modeling the post-shock flow follows.

2.2. *Evolution of Shocked Gas*

As we are mainly interested in the region of shocked gas between the two stars, we briefly review here the jump conditions for a radiative shock, which will form the backdrop of our further analysis.

2.2.1. *Jump Conditions*

The conditions behind a radiative shock front are largely described by the Rankine-Hugoniot jump conditions, with only a change to the energy equation as the downstream gas is allowed to cool and radiate energy away. The jump conditions are given here in 1D, with ρ_0, u_0, P_0 as the pre-shock gas conditions, and ρ_s, u_s, P_s for the post-shock gas.

$$\rho_0 u_0 = \rho_s u_s \tag{5}$$

$$\rho_0 u_0^2 + P_0 = \rho_s u_s^2 + P_s \tag{6}$$

$$\rho_0 u_0 \frac{d\epsilon}{dx} + P\frac{du_0}{dx} = -\rho_s L \tag{7}$$

Here L is the cooling function in units of energy per unit mass per unit time.

To describe the evolution of the shocked and cooling gas in the wind interaction region, we follow Sarangi and Slavin (2022), solving the 1D shock equations and using the formalism of Shull and Draine (1987); Dopita and Sutherland (2003). Accounting for the radiative losses in the energy equation, we describe the evolution of the temperature and density behind the shock in terms of the cooling rate, $\eta(T)$:

$$\frac{d\rho}{dt} = \frac{\rho\eta(T)}{\rho_0 v_s^2}\left(\frac{5}{2} - 4\frac{\rho_0}{\rho}\right)^{-1} \tag{8}$$

$$\frac{T}{T_0} = (1+M^2)\frac{\rho_0}{\rho} - M^2\frac{\rho_0^2}{\rho 2} \tag{9}$$

where M is the isobaric mach number:

$$M^2 = \frac{\rho_0 v_s^2}{P_0} \tag{10}$$

The cooling rate, $\eta(T)$ in [ergs cm^{-3} s^{-1}] is found as:

$$\eta(T) = n_e \sum_i n_i \Lambda_i(T) \tag{11}$$

$$n_e = \sum_i \sum_l l f_{i,l} n_i \tag{12}$$

$$\Lambda_z = \frac{\sum_i n_i \Lambda_i}{\sum_i n_i} \tag{13}$$

where $f_{i,l}(T)$ is the fractional ionization of a given element i in the gas at a temperature T and ionization state l. n_i is the number density of that element in the gas, and n_e is the electron number density. The cooling function, $\Lambda(T)$ in [ergs cm^3 s^{-1}], is calculated using `CLOUDY` (Ferland et al. 2013) for each constituent element in the gas. We consider here three cases: 1. A gas composed of solely WR elemental abundances, 2. A gas of solely OB elemental abundances and 3. A gas composed of fully mixed WR and OB gas abundances. These abundances are listed in Table 2. The pure WR gas case acts as an 'upper bound' on the amount of cooling, as it is the most metal-rich case we examine, with an extreme carbon abundance. The actual shocked gas in the system will not be composed purely of the material from one of the stars, as there are known instabilities in this system, such as the Kelvin-Helmholtz instability and the thin-shell instability (Parkin and Pittard 2008) which will cause mixing of the material between the stars. The extent of that mixing depends sensitively on how these instabilities manifest, and we will examine this in future work. In this initial study, we prescribe the amount of mixing, and take as an example a fully mixed gas.

The cooling functions per element as calculated with `CLOUDY` are shown in Figure 3 and the total cooling rate for the pure WR gas case, a pure OB gas and the fully mixed OB + WR gas cases are shown in Figure 2.

We consider the evolution of a single parcel of gas as it encounters the shock, is compressed, heated, and eventually cools. When this gas parcel is first shocked, it will reach the 'jump temperature' T_j (Raymond 2018), given by:

$$T_j = \frac{3}{16} \frac{\mu m_H}{k} v_s^2 \tag{14}$$

$$\mu(T) = \frac{\sum_i A_i n_i}{\sum_i \sum_l (l+1) f_{i,l}(T) n_i} \tag{15}$$

where μ is the mean particle mass, m_H is the proton mass, and k is the Boltzmann constant. As $\mu(T)$ is itself a function of temperature, illustrated in Figure 4, it is not feasible to use Equation 15 to find the jump temperature. However, as can be seen from the figure, at gas temperatures of order 10^6 K, the gas is fully ionized and

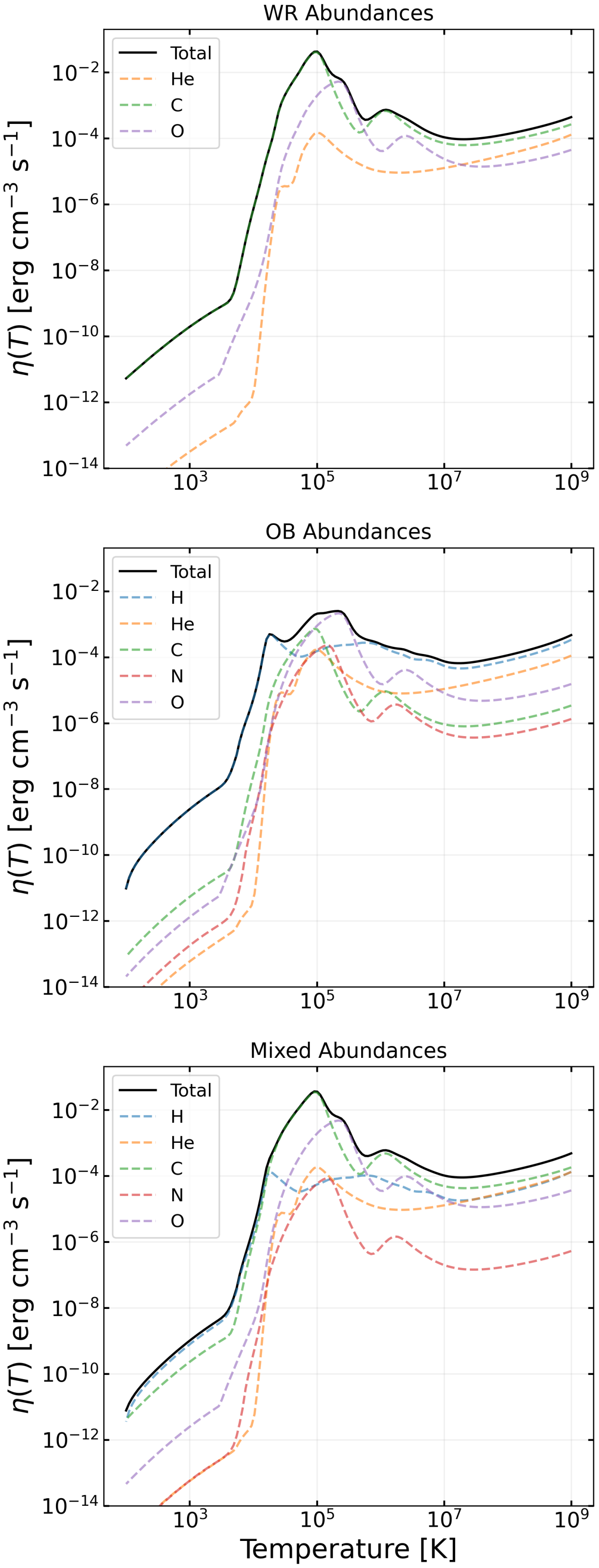

Figure 2. Cooling rates, generated using Cloudy as in Sarangi and Slavin (2022). Top: Cooling rates for gas of only WR abundances. Middle: Cooling rates for gas of only OB abundances. Bottom: Cooling rates for gas of fully mixed WR + OB abundances.

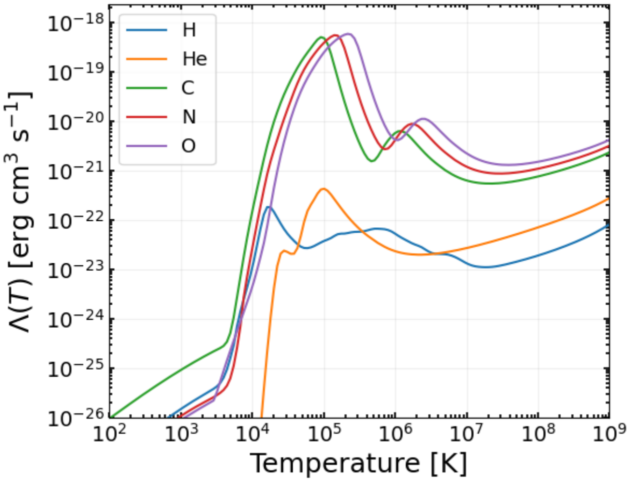

Figure 3. Cooling functions calculated with `CLOUDY`, $\Lambda_i(T)$ for the main constituent elements of WR and OB stellar material

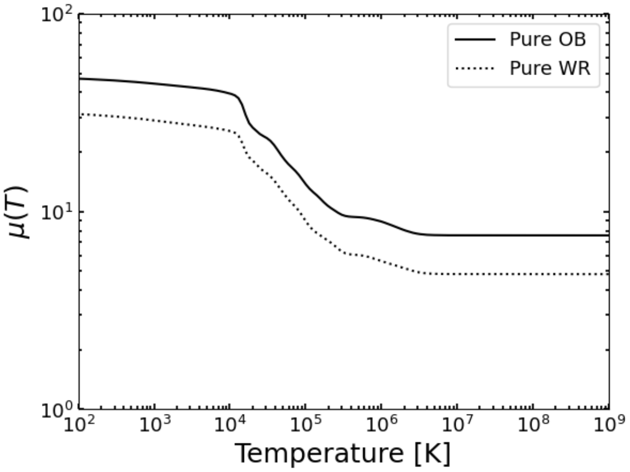

Figure 4. Mean particle mass as a function of temperature for a pure OB stellar material gas, and a pure WR gas. For both cases, the gas is fully ionized by $\sim$ 1e6 K.

$\mu(T)$ has reached a steady value. As our jump temperatures are $\sim 10^8$ K, we use the constant, fully ionized value of μ to determine our jump temperature for each gas composition.

2.2.2. *1D model*

To model the compression and cooling of the gas in the wind collision region, we determine the initial conditions for a single parcel of gas beginning either at periastron or apastron. We find the initial density assuming a constant stellar wind given by $v_{\infty,\mathrm{WR}}$ and a constant mass loss rate of $\dot{M}_{\mathrm{WR}}$. For both systems considered here the values of these parameters that we adopt from the literature are given in Table 3.

Element	OB	WR 140	Mixed
X_H	0.705	0.000	0.352
X_{He}	0.275	0.546	0.410
X_C	0.003	0.400	.0201
X_N	0.001	0.000	0.005
X_O	0.010	0.050	0.030

Table 2. Abundances for the OB and WR stars considered here, from Eatson et al. (2022). Mixed abundances are a 50/50 mixture of each gas.

We then find the immediate post-shock gas temperature and density using the jump conditions described above. We then use Equations 8 and 9 to determine the evolution of the temperature and density. In considering this evolution, we must take into account that the parcel of gas is not static behind the shock. After the gas is shocked, it will follow the fluid flow along the contact discontinuity and away from the immediate interaction zone (Parkin and Pittard 2008; Cantó et al. 1996). As the gas moves, it will also expand, decreasing the density even as the cooling and compression continues. We include this interplay between expansion and compression using the outputs of a 3D hydrodynamic simulation of binary stars and their wind collision region run using `Arepo` code. `Arepo` solves the hydrodynamic equations on an unstructured Voronoi mesh using a second-order finite volume scheme (Springel 2010; Springel et al. 2019). To understand the evolution of the gas, we take a snapshot from the simulation and determine the gas velocity and density at points within the wind interaction region at sequentially larger radial distances from the initial interaction point. As we assume this system in a steady state, the characteristics of a parcel of gas at each of these points also describes the characteristics of one parcel of gas over time. To this end, we fit a power law to the change in velocity and in density with radial distance. We find that the velocity does not change significantly, whereas the density decreases as r^{-2}, as one would expect for a flow due to a constant wind. With these relationships, we can then determine the amount of expansion of the gas at each time step in our 1D model. Gas quantities are evolved as:

1. Set up a range of temperature values, beginning at T_j, evenly log-spaced down to T = 100 K
2. Assuming a constant Mach number, evaluate Equation 9 to determine the new compressed density
3. Using the new temperature and density, lookup and interpolate the appropriate value of $\eta(T)$

WR 104		WR 140	
Parameter		Parameter	
T_{WR}	45,000 K [1]	T_{WR}	57,000 K [8]
M_{WR}	10 $M_\odot$ [2]	M_{WR}	10 $M_\odot$ [7]
L_{WR}	40,000 $L_\odot$ [1]	L_{WR}	930,000 $L_\odot$ [8]
$R_{*,WR}$	6 $R_\odot$ [10]	$R_{*,WR}$	9.79 $R_\odot$ [8]
$\dot{M}_{WR}$	$3 \times 10^{-5} M_\odot \mathrm{yr}^{-1}$ [4]	$\dot{M}_{WR}$	$5.6 \times 10^{-5} M_\odot \mathrm{yr}^{-1}$ [6]
v^∞_{WR}	1.22×10^3 km s^{-1} [3]	v^∞_{WR}	2.86×10^3 km s^{-1} [6]
T_{OB}	30,000 K [4]	T_{OB}	36,000 K [8]
M_{OB}	20 $M_\odot$ [5]	M_{OB}	29 $M_\odot$ [7]
L_{OB}	80,000 $L_\odot$ [4]	L_{OB}	500,000 $L_\odot$ [8]
$R_{*,OB}$	13.5 $R_\odot$ [10]	$R_{*,OB}$	18.2 $R_\odot$ [7]
$\dot{M}_{OB}$	$6 \times 10^{-8} M_\odot \mathrm{yr}^{-1}$ [4]	$\dot{M}_{OB}$	$1.6 \times 10^{-6} M_\odot$ yr^{-1} [9]
v^∞_{OB}	2×10^3 km s^{-1} [4]	v^∞_{OB}	3.20×10^3 km s^{-1} [6]

Table 3. Stellar parameters used in this work, adopted from the literature. [1] Crowther (1997) [2] Sander et al. (2012) [3] Howarth and Schmutz (1992) [4] Harries et al. (2004). [5] Fierro et al. (2015) [6] Williams (2011) [7] Thomas et al. (2021) [8] Lau et al. (2023) [9] Williams et al. (1990) [10] Soulain et al. (2023)

4. Integrate Equation 8 to find the time it takes to cool to this temperature and density
5. Multiply this cooling time by the constant fluid velocity behind the shock to find the distance traveled by a parcel of gas in this time
6. The new density is now the compressed density multiplied by an expansion factor $\propto r^{-2}$

For dense, metal rich gas such as that behind the wind interaction shocks, cooling can be very effective, reducing the temperature to below that of the ambient medium within $\sim$ 10s of days. The top panel of Figure 5 illustrates this for the case of WR140, when the interaction happens at periastron. The situation is very similar for WR104, as in the bottom panel of Figure 5, though the cooling time is roughly twice as long. WR104 has a very circular orbit, meaning the stellar winds are constantly strongly interacting, compared to WR140 in which the orbit is very eccentric leading to periods of strong wind interaction only near periastron. However, the mass loss rates in the WR104 system are somewhat smaller than those in WR140, producing a lower preshock density. This lower density, even when compressed by the shock, leads to less efficient cooling than in the WR140 case, as the cooling rate η is proportional to n^2.

2.2.3. *Radiation and Heating*

The cooling times discussed above consider the shock compression and atomic cooling of the gas, as well as the expansion of the gas over time. However, these gas parcels are also in the strong radiation field of the massive stars in the binary and will be subject to both heating and ionization. We must then consider the energy change in the gas as a combination of the cooling rate, $\eta(T)$ and the heating rate, $\mathcal{H}(T)$. The effects of this radiation field depend on the stellar luminosity an the shape of the stellar spectrum. We model the incident stellar spectrum as a blackbody at the temperature of the stellar photosphere, given in 3. However, the actual radiation field affecting the gas parcels does not have a simple analytical formulation, as it depends on not only the incident radiation but also the effects of radiative transfer between the stellar source and the gas column of wind-driven mass loss between that source and the shocked gas. For our shocked parcels of gas, we must consider the flux of incident radiation that has passed through an increasing column density of gas as it moves through the system. The composition of the gas parcel itself is also important, as the various species in the gas will have different responses to heating and ionization. To capture the effects of the radiation field on our gas, we use the spectral synthesis code `CLOUDY` (Ferland et al. 2013; Chatzikos et al. 2023).

The gas immediately post shock is heated to very high temperatures, where the cooling rate is most efficient, as seen in 2. As the gas is cooled to temperatures $\sim$ 1e4 K however, the cooling rate and the ionization fraction drop off significantly, allowing the heating and ionizing radiation to play an important role in the gas evolution. We use the analytical equations 9 and 8 to describe the gas in the temperature range T_j - 1e4 K, using `CLOUDY` to follow the evolution at lower temperatures. While `CLOUDY` is not intended to follow the time evolution of a gas with this many competing effects on column density, we can use it to determine the heating and cooling on a specific parcel at a given moment in time assuming that the parcel will reach thermal equilibrium. We pro-

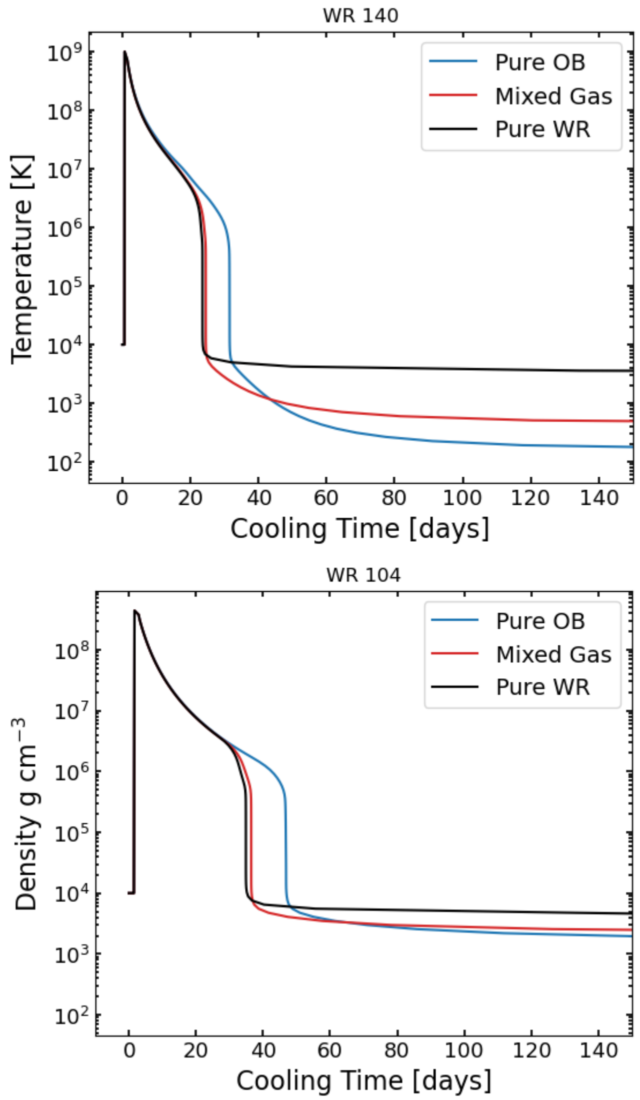

Figure 5. Top: Temperature over time for WR140, at periastron, comparing the cooling time of a pure OB star abundance gas, a pure WR gas, and the fully mixed case. Bottom: The same, for WR 104 at periastron. The mass loss rates in the WR104 system are slightly smaller than those in WR140, leading to smaller gas densities and thus less efficient cooling.

vide initial gas conditions to cloudy using the output of our 1D model above, selecting the gas density and constituent number density when the 1D model has reached 1e4 K.

Our systems are on the extreme ends of density and luminosity for which `CLOUDY` was designed. As such, it is not able to consistently model the gas very close to the star. We thus set the initial distance from the radiation source to be 1e14 cm. However, at this distance from a star with a constant mass loss, there is already some column density of material between the star and the gas parcel we follow, which will attenuate the incident flux. To avoid overestimating the heating on our gas parcel, we first use the spectral synthesis capabilities of cloudy to determine to what extent the stellar radiation will be attenuated. We begin by finding the column density between the star and the shocked gas parcel considering a constant mass loss rate and the radial distance of the gas parcel at the time that it reaches T = 1e4 K. We then set the initial stellar temperature and luminosity, and determine the total transmitted luminosity and shape of the spectrum after passing through the calcu-

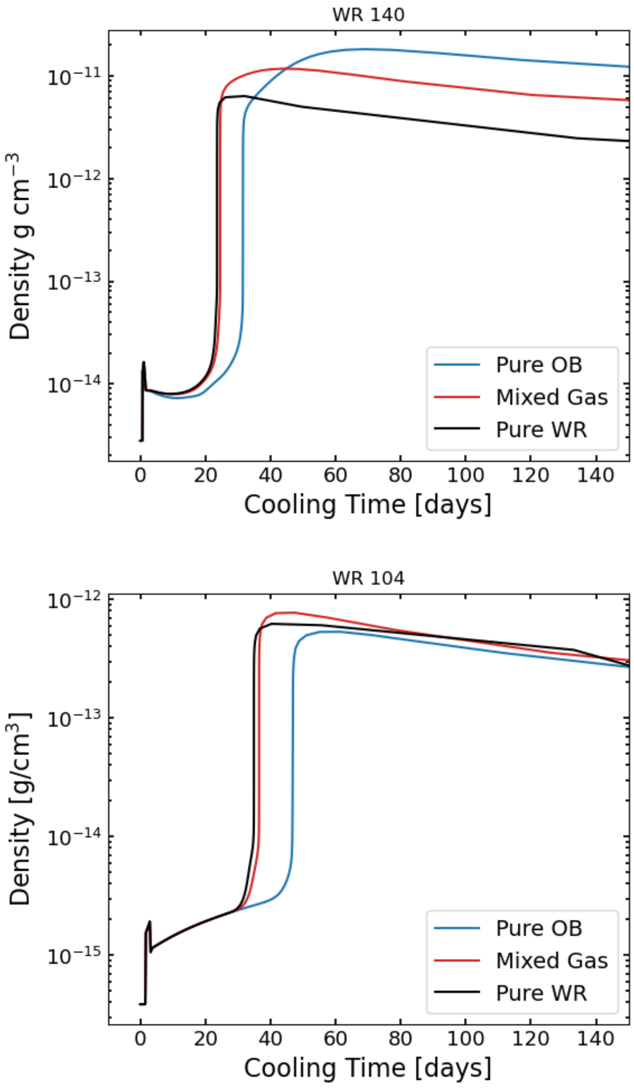

Figure 6. Top: Density over time for WR140, at periastron, comparing the cooling time of a pure OB star abundance gas, a pure WR gas, and the fully mixed case. Bottom: The same, for WR 104 at periastron. The density in each case reaches a plateau as the effects of shock compression compete with the gas expansion as the parcel moves outwards.

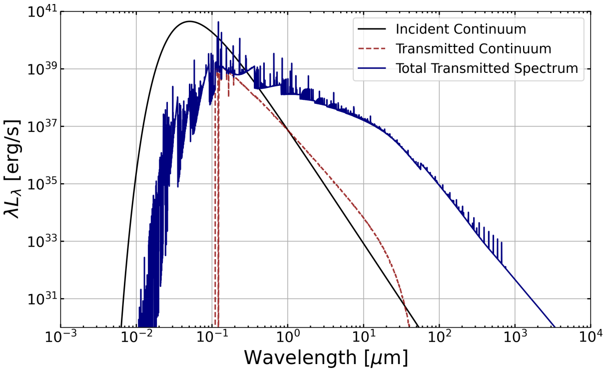

Figure 7. Incident Vs Transmitted Spectrum from `CLOUDY` for WR140. The incident spectrum is strongly peaked in the UV, while the transmitted spectrum has been reddened by it's passage through the mass-loss driven column density between the source and our shocked gas parcel of interest.

lated column density, illustrated for WR140 in Figure 7.

The transmitted spectrum at this distance is then used as the incident spectrum on the shocked parcel of gas. We then use `CLOUDY` to determine the distance at which the gas will have cooled to 2000 K, as we are most interested in the dust formation processes that will begin around this temperature. Another advantage of using `CLOUDY` beyond the inclusion of heating is the molecular formation functionality. As the WR star has been stripped, it has a much higher C/O ratio than solar. This will lead to efficient CO molecule formation, which then provides an effective cooling mechanism. The cooling functions we use at higher temperatures do not take into account molecular cooling, which is expected to be an important factor in our gas. While the code will effectively form CO molecules, it does not reliably track the cooling from these molecules at the low temperatures we are interested in. To correct for this we turn off CO cooling within `CLOUDY`, and include an 'extra' cooling function, a functionality provided for in the code. To determine the appropriate amount of CO cooling for our gas, we follow the prescription in Neufeld and Kaufman (1993), described below.

2.2.4. *Analytic CO cooling function*

Neufeld and Kaufman (1993) treat the radiative cooling of warm (T $\gtrsim$ 100 K) molecular gas. The authors numerically calculate the cooling of multiple molecules, and then present analytic fitting functions. Their functions are most appropriate for temperatures between 3500 K and 100 K, which is somewhat lower than our initial temperature of 1e4 K. As the functions given depend on the H2 column density, we may overestimate the cooling at higher temperatures. As such, a fully self-consistent treatment of CO cooling at temperatures between 1e4-1e3 K would be a significant improvement to our model but is outside the scope of this work.

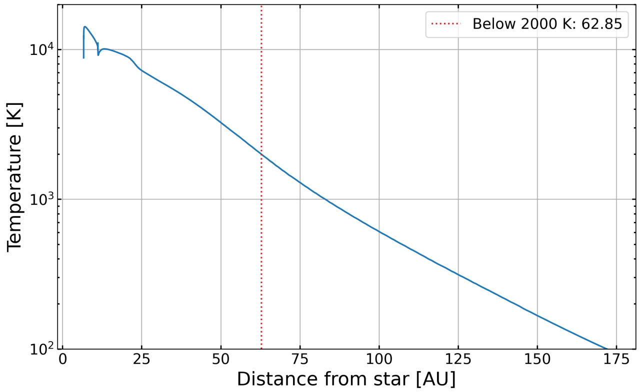

Figure 8. `CLOUDY` output describing the temperature of a gas parcel of pure WR gas composition as a function of distance from the WR star in AU. Considering the atomic and molecular cooling, the density compression and expansion as well as the heating and ionization, we find that the gas will have cooled to temperatures able to begin dust formation at $\sim$ 30 AU.

To make use of these CO cooling functions, we use their reported fits to the density dependence of the cooling function or cooling rate coefficient:

$$\frac{1}{\Lambda} = \frac{1}{\Lambda_0} + \frac{n(H_2)}{\mathcal{L}_{\mathcal{LTE}}} + \frac{1}{\Lambda_0}\left[\frac{n(H_2)}{n_{1/2}}\right]^{\alpha}\left(1 - \frac{n_{1/2}\Lambda_0}{\mathcal{L}_{\mathcal{LTE}}}\right) \quad (16)$$

where Λ_0 is the cooling rate coefficient in a low density limit, and is a function of temperature only. $\mathcal{L}_{\mathcal{LTE}}$ is the luminosity per cooling molecule when the level populations are in LTE, and $n_{1/2}$ is the H_2 density at which the cooling rate coefficient falls below $1/2\Lambda_0$. Values for these quantities for CO specifically are provided in their Table 3, and are organized according to another parameter related to the geometry of the system: $\tilde{N}$. For a spherical stellar outflow with a mass loss rate, this parameter can be found as:

$$\tilde{N} = 1.7 \times 10^{17} \frac{\dot{M}_{-5}^{1/2}}{v_6^{3/2}} \left(\frac{n(H_2)}{\mathrm{cm}^{-3}}\right)^{1/2} [\mathrm{cm}^{-2} \text{ per km s}^{-1}] \quad (17)$$

With the inbuilt `CLOUDY` CO cooling turned off and the analytic functions entered in its place, we then find the distance at which our gas will cool to temperatures appropriate for dust formation. An illustration of this for the WR140 system is in Figure 8.

3. DUST PRODUCTION

The initial formation of dust grains depends on molecules nucleating from the gas phase, and condensation onto those initial cores. The initial gas phase nucleation is the limiting rate in these reactions (Sarangi et al. 2018). Modeling the formation of these initial cores requires a non-steady state, chemical kinetic approach which considers each possible pathway for dust formation and the range of elements available in the gas. In Sarangi and Cherchneff (2013), this process was considered for SN ejecta considered to be in stratified zones. We follow that formalism here, as the constituent elements in our WR gas are extremely similar to the composition of the He/C shell of a Core Collapse Supernova. We will discuss here the most important reactions for this study, and leave an exhaustive accounting of all chemical reactions included in the network to Table 10 in the Appendix of Sarangi and Cherchneff (2013). We discuss below the dust formation for the Pure WR gas abundances case, then the pure OB gas abundances case, and finally the fully mixed case.

3.1. *Pure WR gas*

As in the He/C shell of a Core Collapse event, the composition of our gas is primarily He and C rich, and extremely depleted in H. This limits the chemical pathways available to form molecules and eventually dust, constraining the species we can expect to form. The WR gas is very carbon rich and relatively poor in Oxygen, thus we expect CO to form rapidly, and quickly lock up the available oxygen, limiting the formation of other O-dependent species. The considerably greater abundance of C compared to O in the gas will leave a significant reservoir of atomic C available to begin forming the C chains that will lead to Amorphous Carbon (AC) dust growth. This same O-poor abundance will directly affect the formation of silicate grains, and we consider forsterite as an example silicate here. The formation of the silicates depends on SiO molecules initially, which will struggle to form as the oxygen is locked into CO.

The condensation of atoms onto these initial molecules then determines the formation of the final dust grains. Given the overabundance of carbon, we expect carbon clusters to form readily, though this formation will be modulated by the similarly high abundance of He in the gas. As in Zone 5, the He/C zone in the SNe ejecta of Sarangi and Cherchneff (2013), we expect that the He will be ionized, and thus can easily destroy the precursors of carbon chains, via reactions such as $He^+ + C_n \rightarrow C_{n-1} + C^+ + He$. Carbon chain formation will then struggle to proceed until the He ion mass has decreased. The lack of He ions combined with the low oxygen content of the gas, preventing further formation of CO molecules, means the carbon chains can then form efficiently. We track the formation of these carbon clusters beginning at the smallest molecules of C_2 and C_3, following their formation up through C_{28}, which we consider to be the initial stage of amorphous carbon dust.

The silicate dust we consider here, specifically $MG_4Si_2O_8$, the smallest dimer of forsterite, depends strongly on the reaction chain starting with SiO + SiO, progressing to Si_2O_3 + Mg. These reactions are suppressed due to the low oxygen content, so we expect any silicate dust formation to proceed slowly and culminate in a far lower dust content than carbon-bearing grains. Indeed, we see that this is true for both WR140, illustrated in Figure 9 and for WR104, in Figure 10. The dust formation for each system is shown at periastron and at apastron, to demonstrate the most extreme cases along the orbit.

Beginning with WR140, at periastron the carbon dust begins forming within 35 days post-shock, and proceeds rapidly, reaching its maximum within 70 days post-shock. This formation timescale, assuming a constant gas velocity, can then be related directly to a formation distance. We find that for AC dust in WR140 at periastron, the dust formation begins at $\sim$ 90 AU from the initial shock, and continues until a maximum at $\sim$ 300 AU. These formation distances are in broad agreement with other estimations of dust nucleation distances around this system, as in Williams et al. (2009). The early carbon dust production occurs due to the high C/O ratio in the gas, and the relatively high temperature at which C molecule formation can take place, near 2500K. This is in contrast to the silicates, which require gas temperatures closer to 1500 K Sarangi and Cherchneff (2013), leading to formation beginning about 320 days post-shock, at which point the gas parcel has moved to just over 300 AU away from the system. At apastron, the stellar wind material has dropped considerably in density, leaving even the shocked gas of a lower density compared to that at periastron. This has consequences on the dust formation, which rely on the high densities to encourage the necessary reactions. In figure 9, the dashed lines represent the dust formation at apastron, and there is a notable offset from the solid periastron lines. At apastron, the carbon dust formation begins at 295 days post-shock, and again reaches a maximum rapidly at 350 days, less than 60 days after formation begins. The silicate precursors also follow the general trend from the periastron case, requiring considerably longer to begin formation than the carbon dust. In the apastron case, silicates don't begin forming until 930 days post-shock, leading to a formation distance that is almost three times as large as in the periastron case. It is important to note that for this system, the shocks are likely to behave adiabatically at apastron rather than radiatively, meaning they are unlikely to provide the cooling and compression required to form dust. Thus, our estimates here of dust formation are an upper limit, describing what dust production could occur under 'ideal' circumstances in this location.

In the much more circular orbit of WR 104, the situation is very similar to WR140 at periastron. The mass loss rates are similar between the WR stars in each system, and the distance of WR104 at periastron, 2.1 AU, is close to that of WR140 at periastron, 1.3 AU. Thus, we see very similar trends in dust production between the two cases. The carbon dust, as before, forms early and proceeds rapidly. Carbon dust formation begins only a few days later in 104 compared to 140, starting at 34 days post-shock, and reaching a maximum at 97 days. With the somewhat lower wind velocities in this system, this relates to a dust formation initial distance of ~ 40 AU, only somewhat higher than the estimates in Soulain et al. (2018); Tuthill et al. (2008). The forsterite begins formation slightly earlier in WR104, at 220 days post shock. This difference is likely due to the lower stellar luminosity in WR104, 4e4 $L_\odot$ compared to the considerably higher 9e5 $L_\odot$ in WR140. There is enough carbon available to begin forming as soon as it has reached cool enough temperatures, but the higher luminosity in WR140 slows the cooling enough to delay the formation of silicates. In WR104, the lower luminosity leads to a steeper temperature drop off, allowing the chemistry leading to the forsterite dimer to proceed sooner.

Because the orbit of WR104 is so circular, with an eccentricity of only 0.06, there is a negligible change in dust production between periastron and apastron. WR140, with its eccentricity of 0.88, shows substantial differences in dust production between the locations. This agrees well with observations of both systems. WR104 is a continuous dust producer, and shows an unbroken 'pinwheel' of dust, indicating that dust is produced throughout the full orbit. We see that borne out here, with dust production changing only marginally between the two extremes. WR104, however, shows crescents of dust shells, with the only visible parts of those shells occurring near periastron. While there will be some dust production along the entire orbit, the dust can only reach appreciable densities when the gas density at the interaction zone is high enough, when the stars are close by.

3.2. *Pure OB Abundance Gas*

For this report, I will present preliminary results for dust formation in each system for the case of pure OB abundances gas. This gas has solar abundances, thus a considerably higher amount of H and a considerably lower C/O ratio. This will then favor the production of silicates over carbonaceous grains, as the initial carbon atoms will be quickly locked into CO molecules, leaving almost no gas phase carbon available for dust nucleation. The higher oxygen content also allows for different chemical pathways than in the pure WR gas, evident

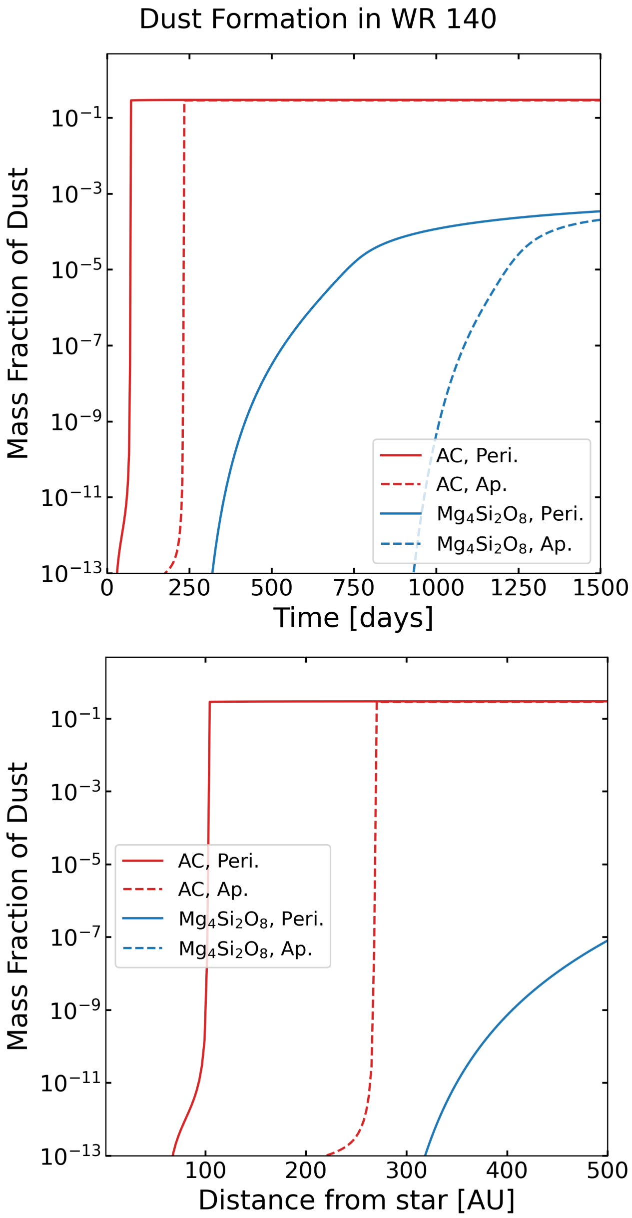

Figure 9. Top: Mass fraction of amorphous carbon dust (red) and forsterite dust precursor (blue) formed over time for WR 140. Bottom: Mass fraction of dust as a function of distance from the WR star. Solid lines indicate dust formation at periastron, dashed lines indicate apastron. Carbon dust forms rapidly in each case, due to the overabundance of gas phase C. The forsterite precursors are delayed in forming due to the lack of O to drive the chemistry, and the maximum is multiple orders of magnitude lower than that of carbon.

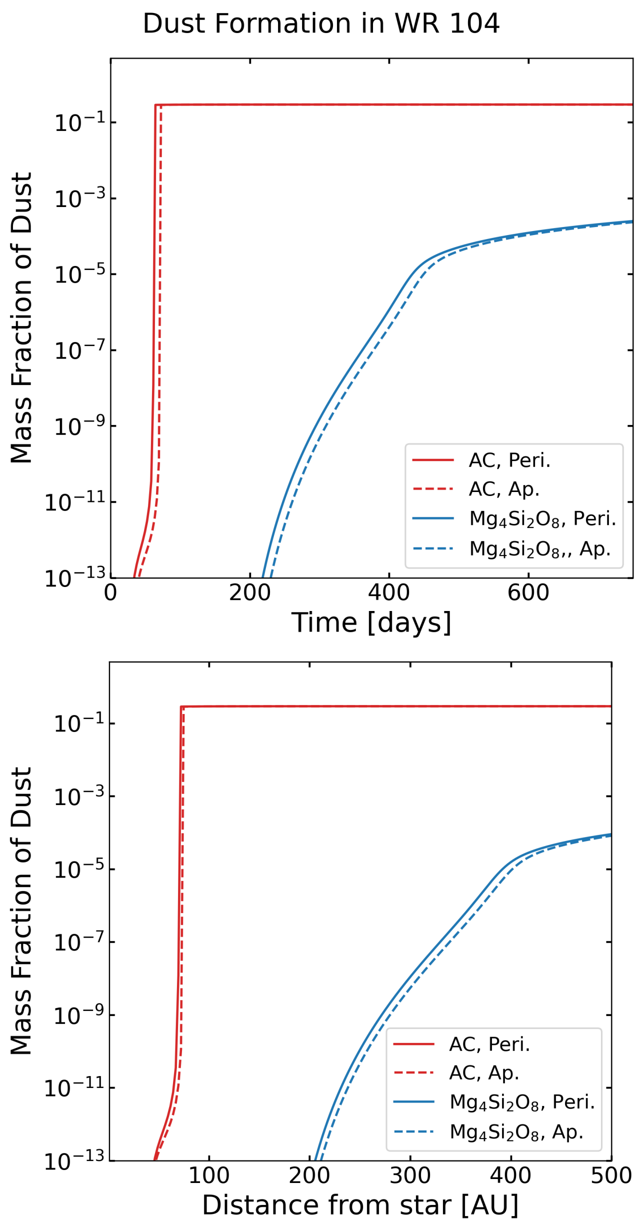

Figure 10. The same as figure 9, but for WR 104. WR 104 has a very circular orbit, leading to only very small changes in dust formation at periastron versus apastron.

in Figures 11 and 12. For both systems, we see that the species of dust which can form are markedly different than in the pure WR case, with the majority of dust in the form of forsterite (MG_2SiO_4), enstatite ($MgSiO_3$) and alumina (Al_2O_3). In the results presented here, we consider the dimers of the forsterite and enstatite, and the tetramer of alumina, Al_8O_3.

Beginning with WR140, in Figure 11, there are two immediate differences from the pure WR case. The carbon dust formation is completely absent, and the only dust species are silicates and alumina. Notably, we also find no dust production at aphelion for this gas composition. This lack of production is related not only to the lower densities at aphelion, as in the pure WR case, but also the lower cooling rates in this gas, delaying the time for the gas to reach the $\sim$ 1500 K necessary to start the silicate-forming reactions. Any delay in cooling time translate also to a greater time for the gas to expand and further lower the density, making dust formation reactions become even less likely. At periastron, dust formation is constrained to silicate species and alumina, all of which are reliant on the oxygen content in the gas. For the silicates, both forsterite and enstatite, their formation process begins with SiO molecule formation, proceeding from SiO + SiO, to Si_2O_2 + SO $\rightarrow$ Si_2O_3, which then further react with Mg to form either enstatite or forsterite. A full accounting of the chemical pathways used to form these materials, and which are included in the dust formation code used here, can be found in Table 10 in Sarangi and Cherchneff (2013).

The formation of alumina depends on the initial formation and dimerization of AlO (Sarangi and Cherchneff 2013). In the OB gas composition case, the much higher O content allows for such oxygen dependent reactions to proceed. While alumina is quite refractory, the abundance of Al in the gas phase is still fairly small so the alumina dust formation process begins at a comparable time to the silicates, but takes longer to reach a non-negligible concentration.

The WR104 case is very similar to WR140 in regards to the species formed and the chemical pathways followed. The major difference in this case is the continued dust production at both periastron and apastron, due to the low eccentricity of the orbit. Unlike in the pure WR case, the dust production is notably smaller at apastron. This is a product of the lower condensation temperature of the silicates and the slightly lower gas density at this point. While this same effect prevented dust production entirely for WR140 at apastron, in this case it only delays formation. However, the delay is long enough to cause what would be an observable asymmetry in the dust spiral around the system, which is not observed. The large formation distances indicated in this case, in the hundreds of AUs, are also not observed. This points to the necessity of mixing of the OB and WR gases in the actual systems.

3.3. *Mixed Abundance Gas*

For the paper resulting from this work, we will also consider the dust production for gas that is an even mixture of OB and WR abundances.

4. SUMMARY AND DISCUSSION

To summarize the findings of this work:

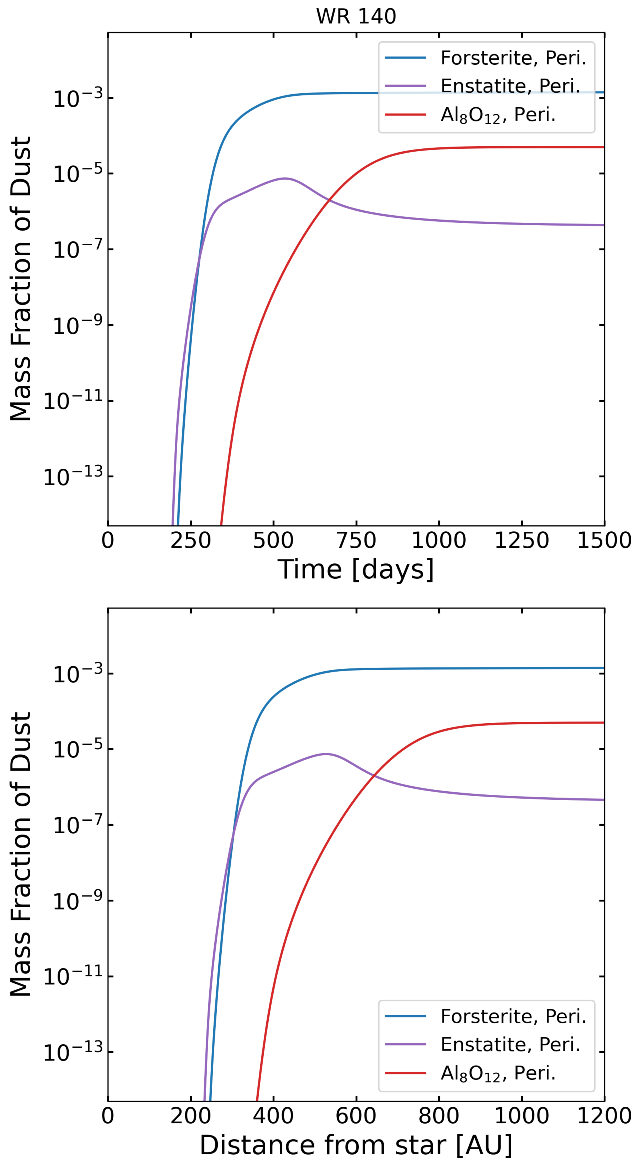

Figure 11. Top: Mass fraction of dust formed over time for WR140. Bottom: Mass fraction of dust as a function of distance from the WR star. The species formed in this case are forsterite (blue), enstatite (purple) and alumina (red). We find negligible dust production at apastron for this case, due both to the lower densities and the longer cooling time.

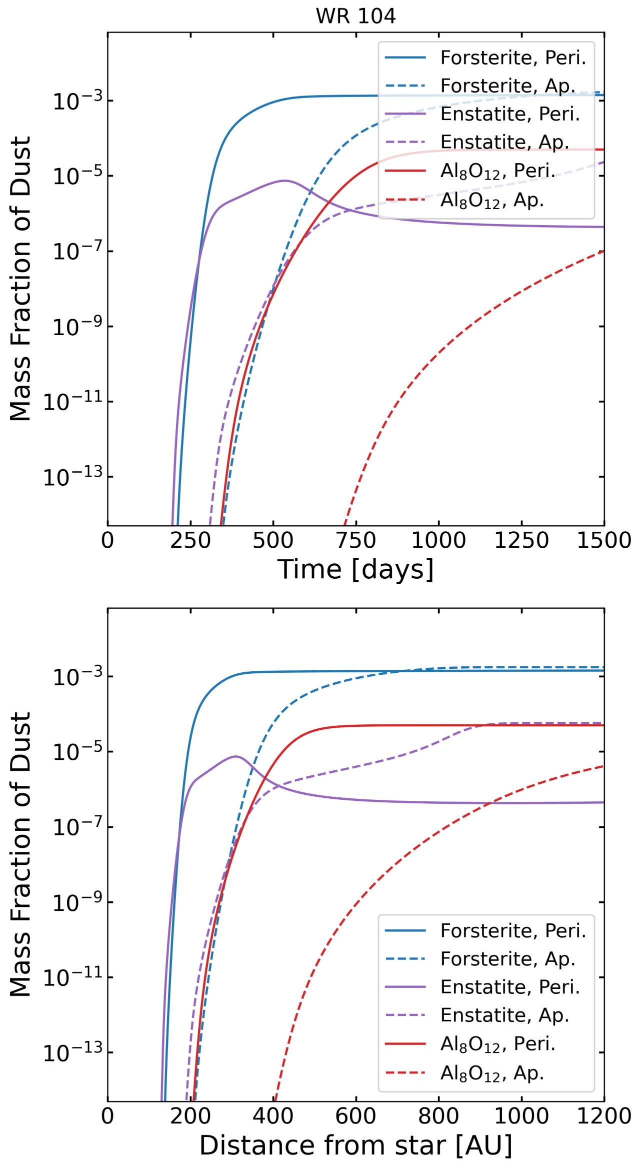

Figure 12. The same as figure 11, but for WR 104. We find the same species of dust form as in the WR140 case, and dust formation at both periastron and apastron. However, the slightly lower density of the gas at apastron does have a noticeable affect on dust production in this case, unlike in the pure WR gas case.

1. In the pure WR gas case, the precursors to amorphous carbon dust form quickly and in a binary manner: once the gas has cooled to 2500 K, the carbon rich environment allows for rapid dust C chain formation, leading quickly to dust. The formation proceeds rapidly until all available C has been locked into clusters.

2. For pure WR gas, The initial dimers for forsterite have their formation greatly delayed compared to carbon. The gas has a small oxygen abundance compared to carbon, so the majority of the oxygen becomes locked into CO molecules as the gas cools, leaving little available for the SiO reactions required to build up silicate grains.

3. Gas of pure OB abundances forms no amorphous carbon grains. The C/O ratio in this gas is less than one, so available carbon is quickly locked into CO molecules and not available for dust formation.

Silicates, now of multiple species, form on the same timescale as in the WR gas cases.

4. The pure OB gas cases, which only make silicates and later Alumina dust, will only have significant dust formation at a much larger radius than is observed around WR binary systems. This implies that some mixing of the stellar material must happen behind the shocks.

5. WR140 shows significant variation in dust production between periastron and apastron. At apastron, the lower initial densities leave both a lower post-shock density and provide less shielding from the extremely luminous WR star. This strong UV radiation prevents cooling and dust formation until the shocked gas has moved a significant distance away from the system.

6. WR104 shows almost no variation in dust production along its orbit, due to the very low eccentricity of the orbit. This aligns well with the unbroken spiral structure of the dust observed for this system.

It is important to mention here that this analysis relies on knowledge of the orbital parameters of the system ad the mass loss rates of both stars. Uncertainties on these properties will directly affect the dust formation timescales and locations. This analysis is also conducted in 1 dimension, assuming spherical symmetry. While this allows us to examine the first order effects on dust formation, it cannot capture the effects of any instabilities, which require higher dimensionality to manifest and understand. There are two instabilities that are likely to be important in these systems: Kelvin-Helmholtz (KH) and the Thin-shell instability.

In colliding wind binaries with unequal wind speeds, as both of our example cases are, the flow velocity along the contact discontinuity is not equal, leaving the system susceptible to KH instabilities that can grow with time. This instability affects another, the ‘Thin Shell Instability’, which is also expected to exist in these systems. This instability, described in Stevens et al. (1992), is related to the winds on either side of the contact being either cooling and adiabatic, or both cooling. In the first case, the cooling winds will result in a dense shell that is bounded by the adiabatic wind on the other side. This shell is found to be unstable, leading to ‘kinks’ in the cooling gas post-shock, which will then be further disrupted by the action of the KH instability. When both winds are radiative, the disruption is on a larger scale, leading to more pronounced Rayleigh-Taylor-esque ‘fingers’ of dense shocked gas. Our one dimensional treatment of the shocked gas here cannot capture the effects of these instabilities. We will examine these effects through 3d simulations in a future work.

Another important caveat to this work hinges on our treatment of the CO cooling in the gas. `CLOUDY` is not designed to compute accurate cooling in a situation as carbon-rich as our gas, thus we rely on an analytic formalism to describe the cooling from CO molecules. This formalism was designed to be used in a less dense medium than what we consider here, thus our exact CO cooling rate may be overestimated by our extrapolation. A self-consistent treatment of CO molecular cooling would be an improvement on this work.

5. FUTURE WORK

For the purposes of this report, I will outline here the planned work to complete this paper. The immediate next step is running the models described above for the case of fully mixed WR + OB gas. The chemical abundances in this gas are significantly different than in the pure WR case and the OB case. The inclusion of H changes the chemical pathways available for dust formation, but the higher concentration of metals also decreases the cooling time. The lower relative abundance of carbon in this case may also affect the rapidity of carbon dust formation.

Following the modeling of the mixed gas case, my conclusions about the reasoning for dust species formation in the OB and mixed cases will need to be discussed with my mentors. While I have relied heavily on Sarangi and Cherchneff (2013) to understand my OB gas composition results, my own understanding of the chemical processes is woefully incomplete. Indeed, one could even say that I have described the preliminary OB results largely on ‘vibes’. And one would be correct.

Further analysis includes determining the length of time of dust production for WR140: for what portion of each orbit is dust expected to form in large enough quantities to be observable? This work will focus on determining at what time from periastron are the stars then separated far enough apart that the density of the shocked material is too low for significant dust production. This separation distance will need to be converted to location along the orbits of the system, for which purpose I have begun to use the orbit integrator `Rebound` (Rein and Liu 2012).

Lastly, I will turn to the problem of converting the current results, given in terms of mass fraction of dust formed, into a more concrete actual mass of dust formed. All of the work so far has relied on modeling of a single parcel of shocked gas, and results describe the mass fraction of dust formed in that parcel. To extend this, I will need to determine the mass of gas contained in the volume of interest between the shocks, which can then be used with the dust formation code results to determine the mass of each species of dust formed. I anticipate using the Arepo simulations to estimate the mass of gas between the shocks, which will rely on finding the locations of the shocks at a given timestep and determining the volume between those shocks. From work so far, I know the distance and time at which dust will begin to form, and how that formation proceeds. This information can provide bounds for determining the location in the simulations of the volume of gas I am interested in. The exact approach for this calculation still requires discussion, and is subject to change based on the advice of my mentors.

This work originated from a project of the Summer Program in Astrophysics 2025 held at the University of Virginia, and funded by the Center for Global Inquiry and Innovation, the National Science Foundation (Grant 2452494), the National Radio Astronomy Observatory (NRAO), the Kavli Foundation and the Heising-Simons Foundation.

REFERENCES

J. Cantó, A. C. Raga, and F. P. Wilkin. Exact, Algebraic Solutions of the Thin-Shell Two-Wind Interaction Problem. *ApJ*, 469:729, Oct. 1996. https://doi.org/10.1086/177820.

M. Chatzikos, S. Bianchi, F. Camilloni, P. Chakraborty, C. M. Gunasekera, F. Guzmán, J. S. Milby, A. Sarkar, G. Shaw, P. A. M. van Hoof, and G. J. Ferland. The 2023 Release of Cloudy. *RMxAA*, 59:327–343, Oct. 2023. https://doi.org/10.22201/ia.01851101p.2023.59.02.12.

I. Cherchneff, Y. H. Le Teuff, P. M. Williams, and A. G. G. M. Tielens. Dust formation in carbon-rich Wolf-Rayet stars. I. Chemistry of small carbon clusters and silicon species. *A&A*, 357:572–580, May 2000.

P. A. Crowther. Remarkable spectral variability in WR 104 (WC9): dust condensation in a hostile environment? *MNRAS*, 290(3):L59–L63, Sept. 1997. https://doi.org/10.1093/mnras/290.3.L59.

P. A. Crowther. Physical properties of wolf-rayet stars. *Annual Review of Astronomy and Astrophysics*, 45(1): 177–219, 2007. ISSN 0066-4146, 1545-4282. https://doi.org/10.1146/annurev.astro.45.051806.110615. URL http://arxiv.org/abs/astro-ph/0610356.

M. A. Dopita and R. S. Sutherland. *Astrophysics of the diffuse universe*. Springer Berlin, 2003. https://doi.org/10.1007/978-3-662-05866-4.

J. W. Eatson, J. M. Pittard, and S. V. Loo. Exploring dust growth in the episodic WCd system WR140. *Monthly Notices of the Royal Astronomical Society*, 517(4): 4705–4713, 2022. ISSN 0035-8711, 1365-2966. https://doi.org/10.1093/mnras/stac3000. URL http://arxiv.org/abs/2204.12354.

G. J. Ferland, R. L. Porter, P. A. M. van Hoof, R. J. R. Williams, N. P. Abel, M. L. Lykins, G. Shaw, W. J. Henney, and P. C. Stancil. The 2013 Release of Cloudy. *RMxAA*, 49:137–163, Apr. 2013. https://doi.org/10.48550/arXiv.1302.4485.

C. R. Fierro, J. Borissova, J. Zsargó, A. Díaz-Azuara, R. Kurtev, L. Georgiev, S. Ramírez Alegría, and F. Peñaloza. Atlas of CMFGEN Models for OB Massive Stars. *PASP*, 127(951):428, May 2015. https://doi.org/10.1086/681703.

R. D. Gehrz and J. A. Hackwell. Circumstellar dust emission from WC9 stars. *ApJ*, 194:619–622, Dec. 1974. https://doi.org/10.1086/153281.

T. J. Harries, J. D. Monnier, N. H. Symington, and R. Kurosawa. Three-dimensional dust radiative-transfer models: the Pinwheel Nebula of WR 104. *MNRAS*, 350 (2):565–574, May 2004. https://doi.org/10.1111/j.1365-2966.2004.07668.x.

I. D. Howarth and W. Schmutz. Near-infrared spectroscopy of galactic Wolf-Rayet stars. *A&A*, 261: 503–522, Aug. 1992.

T. Kato, K. Haseda, H. Yamaoka, and K. Takamizawa. Discovery of Extremely Large-Amplitude Quasi-Periodic Photometric Variability in a WC9-Type Wolf-Rayet Binary, WR 104. *PASJ*, 54:L51–L54, Aug. 2002. https://doi.org/10.1093/pasj/54.4.L51.

A. Lamberts, G. Dubus, G. Lesur, and S. Fromang. Impact of orbital motion on the structure and stability of adiabatic shocks in colliding wind binaries. *A&A*, 546: A60, Oct. 2012. https://doi.org/10.1051/0004-6361/201219006.

R. M. Lau, J. J. Eldridge, M. J. Hankins, A. Lamberts, I. Sakon, and P. M. Williams. Revisiting the Impact of Dust Production from Carbon-rich Wolf-Rayet Binaries. *ApJ*, 898(1):74, July 2020. https://doi.org/10.3847/1538-4357/ab9cb5.

R. M. Lau, J. Wang, M. J. Hankins, T. Currie, V. Deo, I. Endo, O. Guyon, Y. Han, A. P. Jones, N. Jovanovic, J. Lozi, A. F. J. Moffat, T. Onaka, G. Ruane, A. A. C. Sander, S. Tinyanont, P. G. Tuthill, G. Weigelt, P. M. Williams, and S. Vievard. From Dust to Nanodust: Resolving Circumstellar Dust from the Colliding-wind Binary Wolf-Rayet 140. *ApJ*, 951(2):89, July 2023. https://doi.org/10.3847/1538-4357/acd4c5.

D. A. Neufeld and M. J. Kaufman. Radiative Cooling of Warm Molecular Gas. *ApJ*, 418:263, Nov. 1993. https://doi.org/10.1086/173388.

E. R. Parkin and J. M. Pittard. A 3D dynamical model of the colliding winds in binary systems. *MNRAS*, 388(3): 1047–1061, Aug. 2008. https://doi.org/10.1111/j.1365-2966.2008.13511.x.

J. C. Raymond. Shock Waves in Supernova Ejecta. *SSRv*, 214(1):28, Feb. 2018. https://doi.org/10.1007/s11214-017-0453-6.

H. Rein and S. F. Liu. REBOUND: an open-source multi-purpose N-body code for collisional dynamics. *A&A*, 537:A128, Jan. 2012. https://doi.org/10.1051/0004-6361/201118085.

C. K. Rosslowe and P. A. Crowther. Spatial distribution of Galactic Wolf-Rayet stars and implications for the global population. *MNRAS*, 447(3):2322–2347, Mar. 2015. https://doi.org/10.1093/mnras/stu2525.

A. Sander, W. R. Hamann, and H. Todt. The Galactic WC stars. Stellar parameters from spectral analyses indicate a new evolutionary sequence. *A&A*, 540:A144, Apr. 2012. https://doi.org/10.1051/0004-6361/201117830.

A. Sarangi and I. Cherchneff. The Chemically Controlled Synthesis of Dust in Type II-P Supernovae. *ApJ*, 776(2): 107, Oct. 2013. https://doi.org/10.1088/0004-637X/776/2/107.

A. Sarangi and J. D. Slavin. Dust Production in a Thin Dense Shell in Supernovae with Early Circumstellar Interactions. *ApJ*, 933(1):89, July 2022. https://doi.org/10.3847/1538-4357/ac713d.

A. Sarangi, M. Matsuura, and E. R. Micelotta. Dust in Supernovae and Supernova Remnants I: Formation Scenarios. *SSRv*, 214(3):63, Apr. 2018. https://doi.org/10.1007/s11214-018-0492-7.

T. Shenar, D. P. Sablowski, R. Hainich, H. Todt, A. F. J. Moffat, L. M. Oskinova, V. Ramachandran, H. Sana, A. A. C. Sander, O. Schnurr, N. St-Louis, D. Vanbeveren, Y. Götberg, and W. R. Hamann. The Wolf-Rayet binaries of the nitrogen sequence in the Large Magellanic Cloud. Spectroscopy, orbital analysis, formation, and evolution (Corrigendum). *A&A*, 641:C2, Sept. 2020. https://doi.org/10.1051/0004-6361/201935684e.

J. M. Shull and B. T. Draine. The Physics of Interstellar Shock Waves. In D. J. Hollenbach and H. A. Thronson, Jr., editors, *Interstellar Processes*, volume 134, page 283, Jan. 1987.

A. Soulain, F. Millour, B. Lopez, A. Matter, E. Lagadec, M. Carbillet, A. La Camera, A. Lamberts, M. Langlois, J. Milli, H. Avenhaus, Y. Magnard, A. Roux, T. Moulin, M. Carle, A. Sevin, P. Martinez, L. Abe, and J. Ramos. SPHERE view of Wolf-Rayet 104. Direct detection of the Pinwheel and the link with the nearby star. *A&A*, 618: A108, Oct. 2018. https://doi.org/10.1051/0004-6361/201832817.

A. Soulain, A. Lamberts, F. Millour, P. Tuthill, and R. M. Lau. Smoke on the wind: dust nucleation in the archetype colliding-wind pinwheel WR 104. *MNRAS*, 518(3):3211–3221, Jan. 2023. https://doi.org/10.1093/mnras/stac2999.

V. Springel. E pur si muove: Galilean-invariant cosmological hydrodynamical simulations on a moving mesh. *MNRAS*, 401(2):791–851, Jan. 2010. https://doi.org/10.1111/j.1365-2966.2009.15715.x.

V. Springel, R. Pakmor, and R. Weinberger. AREPO: Cosmological magnetohydrodynamical moving-mesh simulation code. Astrophysics Source Code Library, record ascl:1909.010, Sept. 2019.

I. R. Stevens, J. M. Blondin, and A. M. T. Pollock. Colliding Winds from Early-Type Stars in Binary Systems. *ApJ*, 386:265, Feb. 1992. https://doi.org/10.1086/171013.

J. D. Thomas, N. D. Richardson, J. J. Eldridge, G. H. Schaefer, J. D. Monnier, H. Sana, A. F. J. Moffat, P. Williams, M. F. Corcoran, I. R. Stevens, G. Weigelt, F. D. Zainol, N. Anugu, J.-B. Le Bouquin, T. ten Brummelaar, F. Campos, A. Couperus, C. L. Davies, J. Ennis, T. Eversberg, O. Garde, T. Gardner, J. G. Fló, S. Kraus, A. Labdon, C. Lanthermann, R. Leadbeater, T. Lester, C. Maki, B. McBride, D. Ozuyar, J. Ribeiro, B. Setterholm, B. Stober, M. Wood, and U. Zurmühl. The orbit and stellar masses of the archetype colliding-wind binary WR 140. *MNRAS*, 504(4): 5221–5230, July 2021. https://doi.org/10.1093/mnras/stab1181.

P. G. Tuthill, J. D. Monnier, N. Lawrance, W. C. Danchi, S. P. Owocki, and K. G. Gayley. The prototype colliding-wind pinwheel WR 104. *The Astrophysical Journal*, 675(1):698–710, 2008. ISSN 0004-637X, 1538-4357. https://doi.org/10.1086/527286. URL https://iopscience.iop.org/article/10.1086/527286.

R. M. T. White and P. Tuthill. Wolf-Rayet Colliding Wind Binaries. *arXiv e-prints*, art. arXiv:2412.12534, Dec. 2024. https://doi.org/10.48550/arXiv.2412.12534.

P. Williams. Results from the 2009 campaign on WR 140. *Bulletin de la Societe Royale des Sciences de Liege*, 80: 595–609, Jan. 2011.

P. M. Williams. Formation of Dust in Hostile Environments — What We Learn from Observing Wolf-Rayet Stars. *Ap&SS*, 251(1-2):321–331, July 1997. https://doi.org/10.1023/A:1000791629735.

P. M. Williams, K. A. van der Hucht, and P. S. The. Infrared photometry of late-type Wolf-Rayet stars. *A&A*, 182:91–106, Aug. 1987.

P. M. Williams, K. A. van der Hucht, A. M. T. Pollock, D. R. Florkowski, H. van der Woerd, and W. M. Wamsteker. Multi-frequency variations of the Wolf-rayet system HD 193793 - I. Infrared, X-ray and radio observations. *MNRAS*, 243:662–684, Apr. 1990.

P. M. Williams, S. V. Marchenko, A. P. Marston, A. F. J. Moffat, W. P. Varricatt, S. M. Dougherty, M. R. Kidger, L. Morbidelli, and M. Tapia. Orbitally modulated dust formation by the WC7+O5 colliding-wind binary WR140. *MNRAS*, 395(3):1749–1767, May 2009. https://doi.org/10.1111/j.1365-2966.2009.14664.x.

V. G. Zubko. On the physical model of dust around Wolf-Rayet stars. *MNRAS*, 295(1):109–118, Mar. 1998. https://doi.org/10.1046/j.1365-8711.1998.29511348.x.